Applied Surface Science Advances 25 (2025) 100674

Contents lists available at ScienceDirect

Applied Surface Science Advances

journal homepage: www.sciencedirect.com/journal/applied-surface-science-advances

Full length article

Enhancing thermoelectric properties of ScN films through twin domains

J. More-Chevalier [a,*], U.D. Wdowik [b,*], J. Martan [c], T. Baba [d,e], S. Cichoň [a], P. Levinský [a], D. Legut [b,f], E. de Prado [a], P. Hruška [a,f], J. Pokorný [a], J. Bulíř [a], C. Beltrami [c], T. Mori [d,e], M. Novotný [a], I. Gregora [a], L. Fekete [a], L. Volfová [a], J. Lančok [a]

[a] Institute of Physics of the Czech Academy of Sciences, Na Slovance 2, 18221 Praha 8, Czech Republic
[b] IT4Innovations, VSB - Technical University of Ostrava, 17. listopadu 2172/15, CZ 708 00 Ostrava-Poruba, Czech Republic
[c] New Technologies Research Centre (NTC), University of West Bohemia, Univerzitni 8, 301 00 Plzen, Czech Republic
[d] International Center for Materials Nanoarchitectonics (WPI-MANA), National Institute of Materials Science (NIMS), Namiki 1-1, Tsukuba, Ibaraki 305-0044, Japan
[e] Graduate School of Pure and Applied Science, University of Tsukuba, Tennodai 1-1, Tsukuba, Ibaraki 305-8671, Japan
[f] Department of Condensed Matter Physics, Faculty of Mathematics and Physics, Charles University, Ke Karlovu 3, 121 16 Prague 2, Czech Republic

ARTICLE INFO

Dataset link: https://asep.lib.cas.cz/arl-cav/cs/detail-cav_un_epca-0602125-ScN-data/

Keywords:
Thermoelectricity
Scandium nitride
Thin films
Seebeck coefficient

ABSTRACT

Tailoring thermoelectric properties of ScN-based materials is of vital importance for their application, particularly at high operating temperatures. Here, we report on the thermoelectric properties of the ScN layers deposited on MgO (001) substrates by the DC reactive magnetron sputtering. The microstructure of the produced thin films is examined by X-ray diffraction and atomic force microscopy, while their chemical composition and contamination by defects are determined by X-ray photoelectron spectroscopy. The effect of temperature on the phonon properties of ScN layers, having implications for their thermoelectric properties, is explored by Raman spectroscopy. The results of our experiments are confronted with those following from the first-principles studies. We find that the ScN/MgO(001) layers with twin-domain structure reveal enhanced thermoelectric properties at elevated temperature as compared to those measured for almost defect- and domain-free layers, namely, enlarged Seebeck coefficient by about 30% and over two and a half times increased figure of merit at 800 K. Therefore, structural twin domains in thin ScN film appear to be a simple and rather stable solution for the improvement of its thermoelectric properties at elevated temperatures.

1. Introduction

In the last decades, the search for sustainable clean energy along with the miniaturization of sensors and electronic circuits has stimulated intense research on thermoelectricity and thermoelectric devices [1–9]. Such devices are usually employed to convert heat into electrical energy as well as for energy harvesting from the environment and/or harvesting of industrial waste heat [10–12]. Recently, thin films of the transition-metal nitrides (ScN, CrN, ZrN, HfN) [13] as well as metal/semiconductor multilayers and superlattices based on epitaxial ZrN/ScN and HfN/ScN [14–18] have drawn much experimental and theoretical interest as they hold considerable promise for thermoelectric applications.

Among transition-metal nitrides with potential application in thermoelectricity, ScN has recently gained considerable attention for its superior refractory properties enabling its operation at high temperatures. Scandium nitride is a rocksalt-structured, narrow-bandgap n-type semiconductor with an indirect $\Gamma - X$ energy gap of ~0.9 eV and a direct $\Gamma - \Gamma$ gap of about 2.2 eV. ScN, belonging to group III (B) nitride semiconductors, can overcome some limitations of group III (A) nitride semiconductors for a variety of applications [19]. This compound is extremely sensitive to defects, especially oxygen impurities [19–23] that can be present in a large amount if ScN is not synthesized in pure ultra-high vacuum conditions. A high concentration of charge carriers (10^{18} – 10^{22} cm^{-3}) and low electrical resistivity (~300 μΩcm) of ScN lead to its high thermoelectric power factor of 2.5–3.3 W m^{-1} K^{-1} [13,19,24–26]. On the other hand, its high thermal conductivity ranging between 10 and 12 W m^{-1} K^{-1} at room temperature in thick (~450 nm) films [27], results in its limited figure of merit (0.2–0.3) [24,26,28]. Such a high thermal conductivity requires reduction to enable the application of ScN as a thermoelectric material. Thus, ScN has been a subject of doping by various elements, e.g., Cr, Nb, Mg or Li [29–32]. This strategy was successful only to some extent, as yielding smaller thermal conductivity of doped ScN films (~2.2 W m^{-1} K^{-1} for $Sc_{1-x}Nb_xN$ with $x = 0.1$), led also to deterioration of its electrical

* Corresponding authors.
E-mail addresses: morechevalier@fzu.cz (J. More-Chevalier), urszula.danuta.wdowik@vsb.cz (U.D. Wdowik).

https://doi.org/10.1016/j.apsadv.2024.100674
Received 18 October 2024; Received in revised form 18 November 2024; Accepted 2 December 2024
Available online 24 December 2024

resistivity and Seebeck coefficient. Recently, the Ar-implanted ScN films have been shown to exhibit improved Seebeck coefficient (−30 to −85 μV K^{-1} at 600 K) due to introduced deep acceptor levels reducing concentration of free carriers [33] as well as strongly lowered thermal conductivity (3 W m^{-1} K^{-1} at 300 K vs 12 W m^{-1} K^{-1} in defect-free ScN) because of a higher level of scattering by defects, i.e., lower phonon mean free path. Several experimental studies performed during the last years on diversely modified ScN showed a large variation in its thermoelectric properties. A better understanding of the properties of ScN in the form of film for its potential application as a thermoelectric material calls for additional investigations that should be carried out for the almost defect-free ScN films, i.e., containing neither added dopants nor implanted elements. Therefore, in the present work the ScN layers deposited on MgO(001) substrates with a thickness of about 1 μm have been prepared. We managed to obtain two kinds of ScN layers, namely, the layer without defects, which is here denoted as ScN, and the second one revealing a twin-domain structure denoted as ScN-T. We examine the microstructure, vibrational and thermoelectric properties of these layers not only at room temperature but also at elevated temperatures up to 800 K. Our experimental research is supported by *ab initio* simulations based on the density functional theory (DFT) employed to explore the thermoelectric properties of an ideal ScN crystal and changes in its phonon dynamics as a function of temperature via *ab initio* molecular dynamics (AIMD).

2. Methodology

2.1. Experimental

The ScN layers were deposited on double-side polished (10 × 10 × 0.5 mm^3) MgO (001) substrates in an ultra-high-vacuum (UHV) system (~10^{-8} Pa) by DC reactive magnetron sputtering using a mixture of Ar (99.9999% pure) and N_2 (99.9999% pure) discharge with a ratio of 60/40, respectively. The MgO substrates (001 oriented, 99.95% purity, from Alineason Materials and Technology) were cleaned using several steps, first with acetone in an ultrasonic bath, then repeated with ethanol and blown dry with an N_2-gun. The sample holder was electrically heated first to be degassed at 573 K for 30 min and then to reach the deposition temperature of 1123 K. Before starting the deposition process, the substrate was kept for 1 h at the deposition temperature for the surface reconstruction process. The temperatures were measured by two thermocouples attached to the sample holder. The working pressure of 2 Pa was used to sputter ScN from three Sc targets (NEYCO: Sc 99.9%) of one-inch diameter with measured contamination of Ta at 0.1%. A sputtering power density of 2.8 W cm^{-2} was used to deposit films with thicknesses of 800 ± 50 nm. The distance between the targets and the sample holder was fixed at 5 cm. The thicknesses were measured by a profilometer. Uninterrupted deposition led to the formation of ScN layers. Conversely, periodic interruption of one cathode every hour during the deposition process produced ScN-T layers.

The X-ray diffraction measurements were performed on three different diffractometers. We measured high-resolution symmetric reciprocal space maps (RSMs) on a Bruker D8 DISCOVER diffractometer with a four-crystal Bartels monochromator and Cu $K\alpha_1$ radiation, high-resolution 2D-RSMs on a SmartLab SE Multipurpose diffractometer (Rigaku Corp., Tokyo, Japan) using Cuα_1 radiation and a 2-bounce Ge (220) monochromator while the $\theta - 2\theta$ scans and pole figures were measured on a PANalytical X'Pert PRO powder diffractometer without any monochromator.

The composition of the films was investigated using X-ray photoelectron spectroscopy (XPS) NanoESCA Omicron instrument. A mono chromatic Al anode K_α radiation was used as an X-ray source. The analyzed spot size was 100 × 300 μm^2 and several positions on the sample were probed. The depth profiling process was described in our previous works [34,35]. Spectra are presented *as measured*, which means that no charge correction was performed. Under these conditions, the binding energy of the *N* 1s peak measured on the surface amounts to 396.0 eV and remains in close agreement with the value reported in other studies [35].

The Raman spectra were recorded in a backscattering and parallel-polarization (VV) configuration using a Renishaw Raman spectrometer (System 1000) equipped with Bragg filters. The spectrometer was calibrated using the silicon F1 g peak at 520.2 cm^{-1}. An Ar-laser with an excitation wavelength of 514 nm, power ~10 mW, and spot size of 5 μm (× 50, NA = 0.55, Olympus microscope objective) was used. The spectra from ScN and ScN-T were scanned at 10 s per frame, × 5 accumulations, in a temperature chamber Linkam HFS600E-PB4 stage at temperatures ranging from 300 to 800 K. The measured phonon modes covered the range of frequencies of 15–1800 cm^{-1}.

An atomic force microscope (AFM Dimension ICON, Bruker) was used to investigate the surface morphology and roughness. The measurements were performed under ambient conditions and images were obtained in the Peak Force Tapping mode using ScanAsystAir tips with scan areas of 4.4 × 4.4 μm^2.

Electrical resistivity and Seebeck coefficient were measured simultaneously using a custom-made instrument which employs the four-probe method. Platinum electrodes were used as current probes and Pt-PtRh (type S) thermocouples served both as voltage probes and to measure the sample temperature and its gradient. Measurements were performed in a nitrogen atmosphere on samples typically 10 mm long and 3 mm wide.

We used two techniques to measure thermal effusivity. In the first one, thermal effusivity in various depths under the sample surface is determined by a measurement system based on pulsed photothermal radiometry described in detail elsewhere [36,37]. This technique uses a pulsed laser to heat the material surface and a fast infrared detector to observe temperature decrease after the laser pulse impact. From the temperature decrease with time in the nanosecond time range, the thermal effusivity in depth of hundreds of nanometers is evaluated. The three-layer 1D model with surface absorption of laser light without thermal interface resistances between layers is employed, as described in Ref. [38]. Semitransparency correction is applied according to Ref. [37]. In the second technique, thermal conductivities in the cross-plane direction of the ScN films are measured with a picosecond thermo-reflectance apparatus (PicoTR, NETZSCH-Gerätebau GmbH) at room temperature [39,40]. Before the measurement, a 100 nm-thick Pt layer is deposited on the films by sputtering. Front-heat front-detect (FF) configuration is applied to the samples and thermal effusivities of the films are determined. To calculate the thermal conductivity, the specific heat capacity and density of the films were assumed to be 846 J $kg^{-1}K^{-1}$ and 4400 kg m^{-3}, respectively.

2.2. Theoretical

Calculations were performed within the framework of density functional perturbation theory (DFPT) implemented in the QUANTUM ESPRESSO (QE) package [41,42]. The Perdew–Burke–Ernzerhof (PBE) generalized gradient approximation (GGA) exchange–correlation functional [43] and the projector augmented wave (PAW) pseudopotentials for the description of the electron–ion interaction were employed. The PAW pseudopotential with 3 and 5 electrons in valence for Sc and *N* atoms, respectively, were adopted from the QE database. A kinetic energy cut-off of 51 Ry was used for the plane-wave basis set. The DFPT was used to determine band structures, phonon dispersions, and the electron–phonon (*e*-ph) coupling matrix elements on a coarse **k** and **q**-point grids of 12 × 12 × 12 and 4 × 4 × 4, respectively. Subsequently, the quantities required to evaluate the *e*-ph self-energy $\sum_{n,\mathbf{k}}^{e-\mathrm{ph}}$ were interpolated on significantly finer 48^3-**k** and 16^3-**q** grids via maximally localized Wannier functions formalism implemented in the electron–phonon Wannier (EPW) package [44–46]. Assuming that the major scattering mechanism is due to the (*e*-ph) interaction, the scattering

rates can be expressed in terms of an effective transport phonon frequency distribution $\alpha^2_{\mathrm{tr}\mathbf{k}}(\omega)F(\omega)$ [47], which was calculated using the EPW code. The *e-e* scattering has been neglected as being usually significantly smaller in comparison with that arising from the *e*-ph mechanism [48,49]. Hence, in the present consideration the calculated resistivity $\rho(T)$, which is determined in the scattering time approximation is related solely to the scattering of electrons by phonons. Also, the computed electronic contribution to thermal conductivity k_e is approximated by $k_{e-\mathrm{ph}}$ and determined via the Wiedemann–Franz law from the electrical conductivity $\sigma(T)$, which is an inverse of $\rho(T)$. The lattice thermal conductivity k_L contains contributions from acoustic k_{La} and optical k_{Lo} phonons, i.e., $k_L = k_{La} + k_{Lo}$. The k_{La} was estimated using the semi-empirical Slack model [50,51], while the k_{Lo} was evaluated according to the approach proposed by Cahill [52,53]. Detailed formulas are given in the Appendix A. To calculate the Seebeck coefficient the BOLTZTRAP2 code has been applied [54].

To study the temperature evolution of the ScN Raman spectra, the AIMD simulations within the isothermal–isobaric (NpT) and canonical (NVT) ensembles were performed using the VIENNA AB INITIO SIMULATION PACKAGE (VASP) [55,56]. Here, also the PAW and PBE exchange–correlation potential were adopted to describe electron–ion interaction. The energy cutoff of 520 eV for the plane wave expansion was applied. Calculations were carried out at the Γ-point for the system consisting of 216 atoms in a cubic supercell. The system was heated from 300 to 800 K with a temperature step of 100 K in the NpT ensemble during 20 ps and subsequently equilibrated at each temperature for 10 ps. The Langevin thermostat was used to control the temperature during the NpT simulations. The shape constraints for the volume fluctuations experienced under Parinello–Rahman dynamics were imposed. Production runs were carried out within the NVT scheme for 20 ps. The temperature was controlled by the Nosé–Hoover thermostat. To compare the results of our AIMD simulations with the measured Raman spectra, the power spectra of the autocorrelation function $G_{\mathbf{k}}(\omega)$ were projected onto the Γ-point of the cubic $Fm\bar{3}m$ structure of ScN. Details of the formalism and applied procedure are provided and widely discussed in the pertinent literature [57,58].

3. Results and discussion

3.1. X-ray diffraction

Symmetric (black curve) and skew-symmetric (red and blue curves) $\theta - 2\theta$ scans of the ScN-T films deposited at 1123 K on MgO (001) substrates are shown in Fig. 1. Peaks marked with (*) and (**) correspond to the Cu K_β reflections from the MgO substrate and ScN-T layer, respectively. The symmetric and skew-symmetric $\theta - 2\theta$ scans of the ScN films are presented in Fig. S1 (supplementary information). No difference between diffraction patterns measured for both samples is observed. The ScN films show a unique reflection at $\chi = 0°$, being due to the 002 orientation which corresponds to the 002 grains epitaxially grown cube-on-cube with respect to the MgO substrates. Similar results have been reported for the ScN films deposited on MgO by different PVD techniques [19,21,24,59–61].

Fig. 2 shows the pole figures of the 002, 022, and 111 orientations of the ScN-T and ScN layers. The center of the 002 pole figure displayed in Fig. 2(a) corresponds to the main 002 orientation peak in ScN-T. Like in our previous work dealing with the ScN films [23], the eight spots at $\chi \approx 48°$ and four at $\chi \approx 70°$ come from four twin domains grown on the 111 twinning planes of the 002-oriented grains. Each twin domain produces three poles (the poles generated by one of those domains have been marked with red circles). Beyond the four intense spots, which are expected for the epitaxial films due to the 001 orientation in a cubic structure, the four extra poles arising from the twins are observed in the pole figures of the 022 and 111 orientations that are shown in Fig. 2(b) and Fig. 2(c), respectively.

The reciprocal space maps (RSM) and the 2D reciprocal space map (2D-RSM) of the ScN-T films are depicted in Fig. 3. For comparison, the RSM and 2D-RSM of the ScN layer are given in Fig. S2 (Supplementary information). The FWHM values of the 002 peak are equal to $K_{2\theta}(002) = 0.364°$ and $K_\omega(002) = 0.596°$. The 2D-RSM shows the different peak positions as well as the peaks from twins in the 111 planes.

3.2. Atomic force microscopy

The images of the ScN-T film surface obtained from the atomic force microscopy confirm the film crystallization that we have observed using X-ray diffraction. Additionally, they reveal two kinds of morphologies mixed in the entire ScN-T surface, as shown in Fig. 4. The first surface, which is shown in Fig. 4(a) is composed of grains with square shapes, while the second one, depicted in Fig. 4(b), consists of grains with 3D-pyramidal shapes. In comparison to the ScN-T film surface, the almost defect-free ScN film surface presents only square shape morphologies equivalent to the one shown in Fig. 4(a).

The flat surface made of square-shaped grains corresponds to the surface for the ScN films oriented 001, whereas the surface presenting isosceles-pyramidal-shape grains reflects 3 surfaces from the family 001 coming from the disoriented crystals through the twinning effect in the 111 planes. The grains with an isosceles-pyramidal shape are rotated by 90° relative to each other, confirming the results from XRD pole figure measurements visible in Fig. 2(a). The measured values of root mean square (RMS) surface roughness amount to 1.4 nm and 93.1 nm for the surface with square shapes and the surface exhibiting 3D-pyramidal-shaped grains, respectively. For comparison, the AFM image of the ScN films is given in supplementary information, Fig. S3. We also note that the formation of a mound structure is a characteristic and very common feature of the ScN as well as other nitride films [21,25,30,59,62,63]. It is connected with the effect of adatom mobility on a film surface ascribed to the presence of defects, which limits the down-step motion of atoms due to the Ehrlich–Schwoebel barrier and favors the uphill migration on terraces [30,64–66]. In the present work, intentional interruptions of one of the cathodes during the ScN-T layer deposition modify the energy landscape for adatoms. This disruption prevents the complete overcoming of the Ehrlich–Schwoebel barrier, leading to the formation of twin domains. As evidenced by X-ray diffraction, the absence of equilateral 3D pyramidal grains characteristic of 111-oriented grains on the mound structures of ScN-T layers confirms the lack of such grains within the layer.

3.3. XPS spectra

Measured XPS spectra of ScN films are displayed in Fig. 5. The presence of all expected elements, O, Sc, N and C, on the surface is confirmed. Based on high-resolution spectra, it is clear that the surface composition corresponds to Sc nitride, Sc oxide and airborne carbon contamination. After the Ar+ depth profiling sputtering, a highly pure ScN material is observed. Carbon contamination disappears and the proportion of oxides is significantly lower; the oxygen concentration in the bulk of the material is below 2.0% atomic. Further, there is a Sc 2p peak broadening and Ar ion implantation as a result of sputtering-induced damage. In summary, in agreement with our previous studies, XPS results confirm surface composition typical for an air-exposed ScN and a high quality of produced ScN films [35]. As regards XPS measurements, there are no apparent differences between the ScN and the ScN-T films.

3.4. Raman spectroscopy

Fig. 6 shows the Raman spectra of ScN and ScN-T measured at the VV polarization and temperatures ranging from 298 to 800 K. In general, the spectra are very similar to those determined in our previous study [23] as well as consistent with the reported Raman spectra of

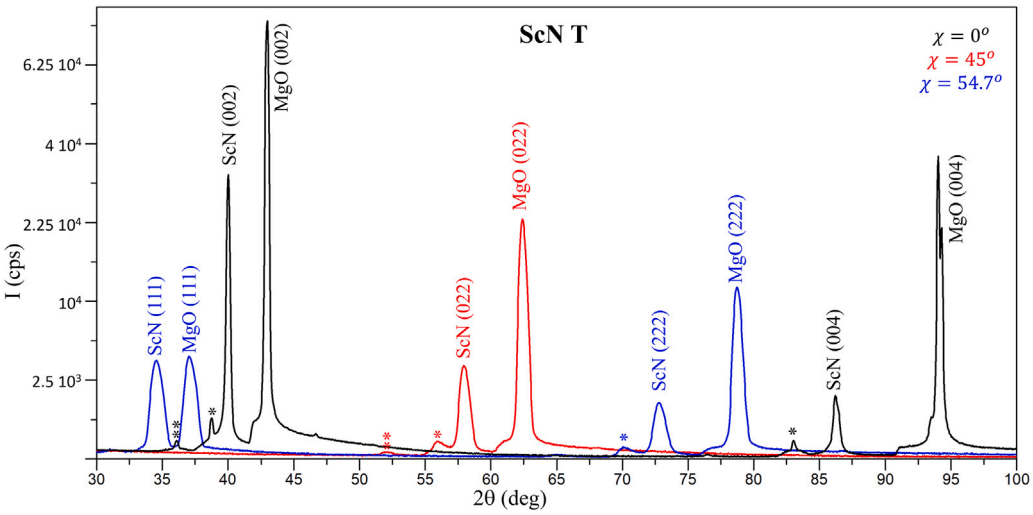

Fig. 1. Symmetric (black curve) and skew-symmetric (red and blue curves) scans in ScN-T films deposited on MgO (001) substrates. Peaks are labeled by their phase and (hkl) indices. Peaks marked with (*) and (**) correspond to the Cu Kβ reflections from the MgO substrate and ScN-T layer, respectively. (For interpretation of the references to color in this figure legend, the reader is referred to the web version of this article.)

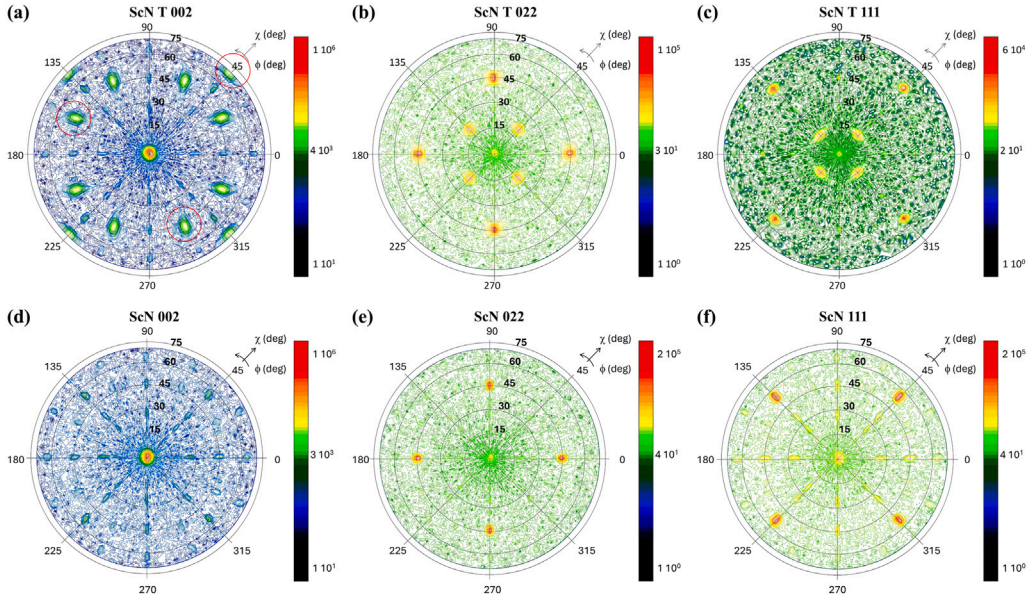

Fig. 2. Pole figures of the 002, 022, and 111 orientations of the ScN-T (a, b, and c) and ScN (d, e, and f) films deposited at 1123 K. The red circles in (a) show the peak positions of one of the twins observed in the figure.

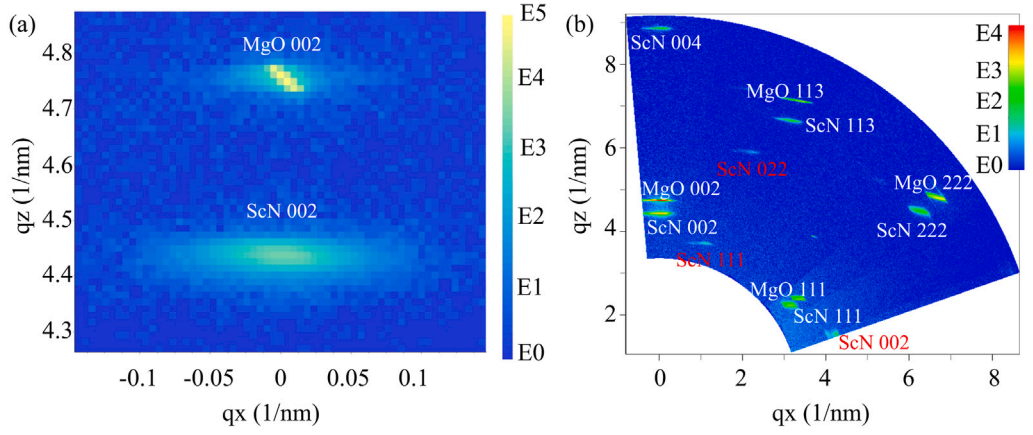

Fig. 3. (a) The 002 reciprocal space map (RSM) and (b) the 2D reciprocal space map (2D-RMS) of ScN-T films. The peaks in the 2D-RMS map denoted in red correspond to the peaks from the twins in the 111 plane.

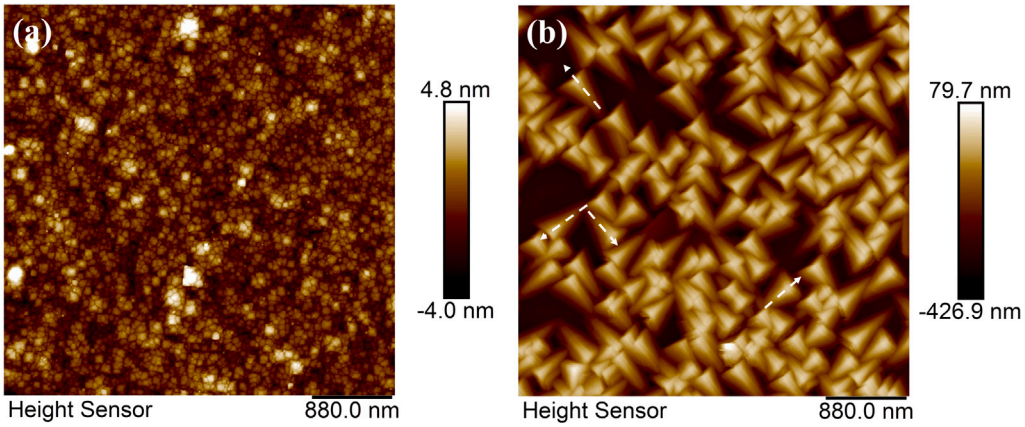

Fig. 4. The AFM images from the ScN-T surfaces. (a) Surface formed by square shapes, (b) surface formed by triangle 3D-pyramidal shapes. The arrows denote rotated grains. The RMS values of 1.4 nm and 93.1 nm are measured for surfaces shown in (a) and (b), respectively.

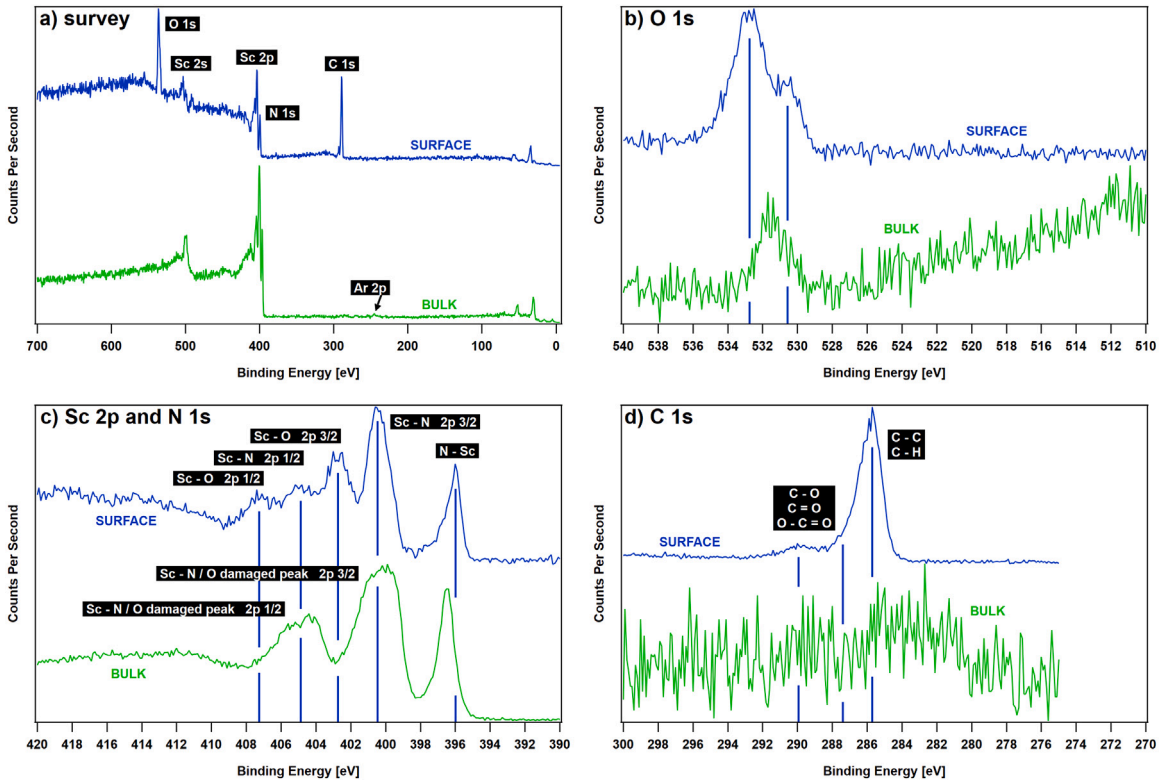

Fig. 5. XPS spectra of ScN film. (a) Survey. Low-binding energy peak labeling is omitted for clarity. (b) O 1s. Surface spectrum consists of two peak components. Bulk spectrum is composed of a single low-intensity peak component. (c) Sc 2p and *N* 1s. Surface Sc 2p is typical with a doublet attributed to Sc–N bonds and a second doublet attributed to Sc–O bonds. Surface *N* 1s consists of a single peak component attributed to N–Sc bonds. Bulk Sc 2p is characteristic of a large FWHM due to sputtering-induced damage. Bulk *N* 1s consists of a single peak component attributed to N–Sc bonds. (d) C 1s. Several peak components form surface C 1s. Bulk spectrum does not show the presence of carbon.

epitaxial ScN layers [67–69]. The main Raman spectrum measured at each temperature covers the energy range extending from 300 to 800 cm^{-1}, while an additional shallow peak observed above 800 cm^{-1} represents the second-order Raman effect.

The Raman spectra of both ScN and ScN-T consist of two, weakly separated broad bands extending between 300 and 550 cm^{-1} and from 550 to 800 cm^{-1}. The lower band is mainly composed of the transverse optical (TO) phonons, whereas the longitudinal optical (LO) modes gather in the upper band. In fact, defect-free ScN should exhibit no Raman-active modes due to symmetry reasons as each atom occupies a site of inversion symmetry. On the other hand, any perturbation and lowering of a local symmetry of the system, which results from the presence of point or extended defects, can lead to the appearance of additional phonon modes, including those Raman or infrared-active. Indeed, the experimental spectra of vacancy-containing, Al- and Ti- or Mg-doped ScN with low content of defects confirm the existence of the Raman modes in this system [23,67–69]. Additional confirmation comes from our AIMD simulations, as illustrated in Fig. 7, which provides temperature behavior of the autocorrelation function power spectra projected onto the Brillouin zone center of the $Fm\bar{3}m$ symmetry ScN crystal.

Although the calculated spectra are obtained for defect-free ScN, the local symmetry of our cubic ScN supercell is no longer of $Fm\bar{3}m$ since the simulations were performed without symmetry constraints imposed on the atomic positions. Therefore, one observes quite broad lower and upper bands, alike in the measured Raman spectra of ScN

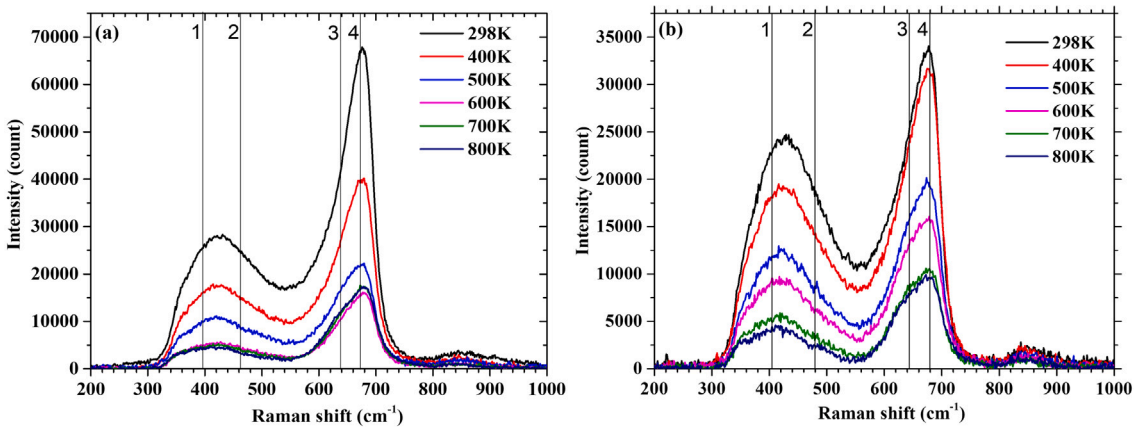

Fig. 6. Temperature evolution of the measured Raman spectra for (a) ScN and (b) ScN-T films deposited on MgO (001) substrate. The spectra are measured at the VV scattering geometry. Baseline corrections are applied. The vertical lines denote the positions of the main fitted peaks for the room temperature spectra. ScN: (1) 404.6 cm^{-1}, (2) 479.9 cm^{-1}, (3) 641.8 cm^{-1}, and (4) 678.8 cm^{-1}. ScN-T: (1) 394.4 cm^{-1}, (2) 462.8 cm^{-1}, (3) 639.3 cm^{-1}, and (4) 676.1 cm^{-1}.

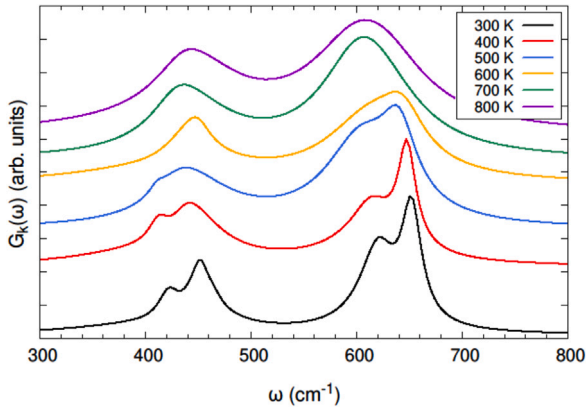

Fig. 7. Calculated wave vector projected power spectra of the autocorrelation function $G_k(\omega)$ onto the Γ-point of the $Fm\bar{3}m$ structure of ScN at temperatures ranging from 300 to 800 K. Positions of peaks at 300 K: ω_1 = 448.4, ω_2 = 457.6, ω_3 = 619.8, ω_4 = 652.1 cm^{-1}.

and ScN-T. These broad bands indicate substantial distribution of the Raman phonons. Actually, both lower and upper spectral bands feature a double-peak structure, which is clearly visible below 500 K in the simulated spectra and it smears out at higher temperatures. The double-peak structure remains, however, less pronounced in the experimental spectra. Nevertheless, the measured spectra of ScN and ScN-T could be fit with four Gaussian profiles, as shown in Fig. S4 and Fig. S5 (Supplementary information). For each temperature, the positions of particular peaks resulting from fits are shown in Fig. 8 as well as they are collected in Table S1 and Table S2 (Supplementary information).

The peaks from the lower band in ScN, denoted as (1) and (2), that arise mostly from the TO phonons, shift their positions downward, i.e., to lower frequencies with increasing temperature T, whereas a slight upward shift is observed for the higher frequency peak (4) belonging to the upper band. Despite some deviation in the vicinity of 500 K, the peak (3) from the upper band practically does not change its position (within the experimental error) with increased T. On the other hand, the behavior of peaks' positions as a function of temperature in ScN-T remains not so clear as in ScN. Only peak (4) tends to increase its position upward, but there is no general trend in the temperature behavior of the remaining peaks, except for a small jump in frequency at 500 K. The observed fluctuations in positions of peaks in ScN-T may result from local microstresses generated by twin domains, while the difference in the respective peaks' shifts between ScN and ScN-T is likely due to much higher concentration of structural defects in ScN-T, which are responsible for the formation of twin domains, as already discussed in the previous sections.

The AIMD simulations also produce shifting of peaks with heating the ScN system, as illustrated in Fig. 9. We observe an almost linear decrease in frequencies of the ω_1, ω_2, ω_3, and ω_4 peaks, albeit with different rates.

The origin of a shift in peak position with temperature, i.e., the change of a phonon frequency, can be manifold. Mostly these are the anharmonic interactions that affect the lattice vibrations. They are responsible not only for the modification of a phonon frequency but also for influencing its lifetime and intensity. Here we limit our consideration to a qualitative description of the effect of temperature on the changes in frequencies of the Raman-active phonons. In principle, the frequency shift of the normal modes with temperature at constant pressure arises from thermal expansion of the lattice Δ_E and pure temperature contribution (phonon–phonon coupling) Δ_A, the latter being due to cubic $\Delta^{(3)}$ and quartic $\Delta^{(4)}$ anharmonicities (three- and four-phonon couplings). Therefore, the temperature dependence of frequency can be written as [70–72]: $\omega(T) = \omega_0 + \Delta_E + \Delta_A$, where ω_0 is the harmonic frequency. In most solids $\Delta_E < 0$, i.e., lattice dilation results in mode softening (red shift). The Δ_E can be evaluated from the following expression:

$$\Delta_E = \omega_0 \left[\exp\left(-3\gamma \int_0^T \alpha(T) dT \right) - 1 \right] \quad (1)$$

$$\Delta_A = \Delta^{(3)} + \Delta^{(4)},$$

with ω_0, γ_i, and $\alpha(T)$ denoting respectively the harmonic frequency, Grüneisen parameter for the optical Raman mode, and the coefficient of linear thermal expansion. The frequency shifts $\Delta^{(3)}$ and $\Delta^{(4)}$ arise from the phonon–phonon interactions due to the lowest-order cubic and quartic terms in the interaction potential. The multi-phonon processes associated with the $\Delta^{(3)}$ usually give rise to a negative frequency shift ($\Delta^{(3)} < 0$), whereas the shift $\Delta^{(4)}$ resulting from the quartic anharmonicity can be either positive or negative [73]. Hence, the overall frequency shift may be either positive or negative, depending on the relative magnitudes of the anharmonic terms in the interatomic potentials and the term following from thermal expansion (volume change).

The simulated Raman spectra that are shown in Fig. 7 contain both Δ_E and Δ_A terms. The contributions $\Delta^{(3)}$ and $\Delta^{(4)}$ appear, however, to be dominated by the thermal expansion term Δ_E, which drives continuous red shift of the optical phonons in ScN, as depicted in Fig. 9. The observed softening of ω_1, ω_2, ω_3, and ω_4 modes follows the temperature behavior of Δ_E predicted for particular peaks, as indicated by the straight dashed lines in Fig. 9. The respective Δ_E shifts were obtained according to Eq. (1), with calculated Grüneisen

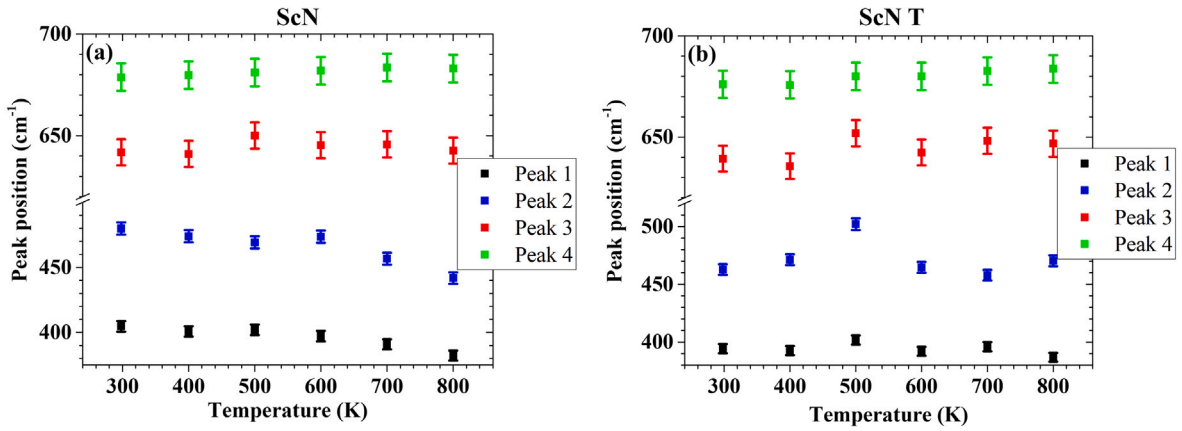

Fig. 8. Positions of the measured Raman peaks in (a) ScN and (b) ScN-T as a function of temperature.

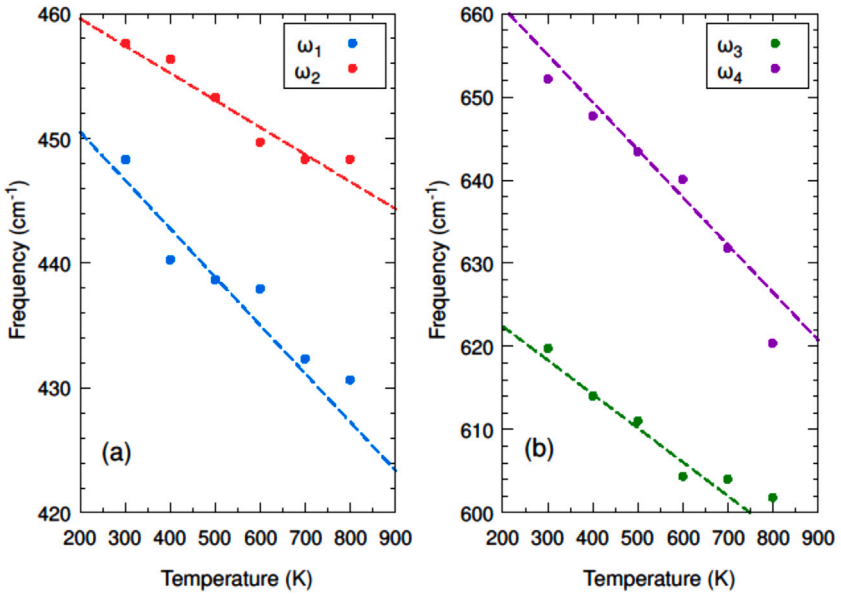

Fig. 9. Temperature evolution of peaks' frequencies in ScN. (a) Positions of peaks ω_1 and ω_2 belonging to the lower band. (b) Positions of peaks ω_3 and ω_4 belonging to the upper band. Dashed lines correspond to Δ_E term evaluated according to Eq. (1).

parameters for the optical Raman modes and by applying the calculated linear thermal expansion coefficient of 7.92×10^{-6} K^{-1}, determined as $\alpha(T) = \frac{1}{3}\beta(T)$, where $\beta(T)$ stands for the volumetric thermal expansion coefficient $\beta(T) = \frac{1}{V}\frac{dV(T)}{dT}$ derived from the NpT simulations. We note the close correspondence between the calculated $\alpha(T)$ and the reported experimental value of $6.61 - 7.98 \times 10^{-6}$ K^{-1} [74,75]. Alike the shifts resulting from the AIMD simulations, the experimental peaks (1) and (2) from the lower frequency band in ScN seem to exhibit similar trends in their position shifts with temperature. Quite the opposite effect is, however, noticed for the peaks (3) and (4) from the upper-frequency band. The former maintains its position almost on the constant level, while the latter one experiences a slight, but visible increase in its frequency (blue shift) with the increasing temperature. Thus, it is likely that the intrinsic anharmonicity due to the quartic term could be indeed strong for the highest phonon frequency band in ScN as it overcomes the sum of $\Delta^{(3)}$ and Δ_E terms. Similarly, the peak (4) in ScN-T reveals a blue shift with temperature, indicating that, also in the twinned-ScN, the quartic anharmonicity plays a significant role in the phonon–phonon interaction, especially among modes with the highest frequencies. It also seems that the interplay between the quartic and cubic contributions in Δ_A and the thermal expansion term Δ_E in ScN-T takes place, and hence the shifts of peaks (1)-(3) do not show straightforward behavior with increasing temperature. In fact, the effect of hardening (blue shift) of the Raman-active phonons as a function of temperature has been less commonly reported [76–78] than the softening (red shift) of such modes [79–84]. The observed blue shift has, however, been assigned to some other effects rather than directly to the anharmonicity of lattice vibrations [76,77]. In both ScN and ScN-T, the higher terms in anharmonicity, i.e., at least a positive quartic term seems to dominate at elevated temperatures for the highest-frequency phonons, suppressing contributions from thermal expansion and the lowest-order cubic term in the interatomic potential.

The temperature evolution of the Raman peak intensities in both ScN and ScN-T follows a typical trend, i.e., a decrease in the intensities of peaks with increased temperature. The Raman scattering intensity is proportional to the population difference between the ground and excited vibrational states, the latter being governed by the Boltzmann distribution function. The population difference decreases as temperature increases and this leads to the reduction of the Raman peaks' intensities. An additional factor lowering intensities of the Raman peaks can be correlated with the increase of the absorption light in ScN, which reduces the number of excited phonon modes [79,80]. Such observation has already been made for V_2O_5, WO_3, and MoO_3. In these oxides the closer the absorption band edge of material to the laser frequency

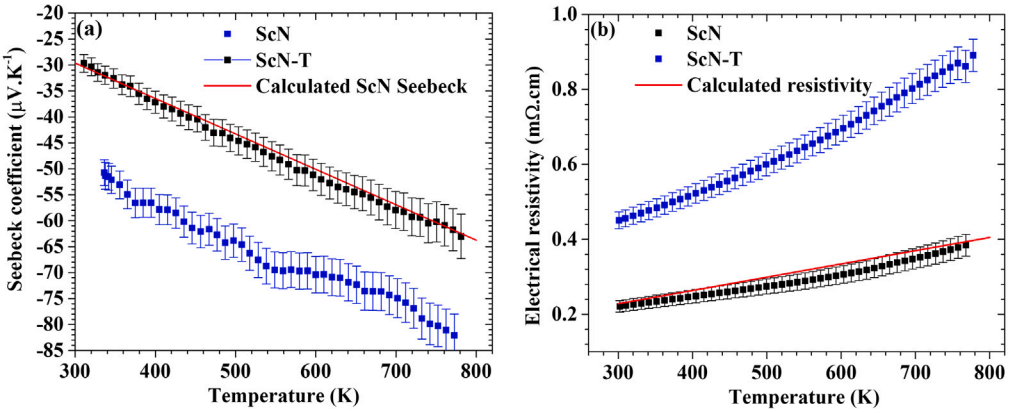

Fig. 10. (a) Temperature dependence of the Seebeck coefficient in ScN and ScN-T layers. (b) Temperature dependence of resistivity in ScN and ScN-T layers. Solid lines represent the calculated Seebeck coefficient and resistivity of ScN.

and the weaker the metal–oxygen bonds, the more meaningful the effect of temperature on the intensity of the Raman spectra [80]. Its band gap (~2.25 eV) lies quite close to the laser incident energy of 514 nm (2.41 eV), which is used in the present Raman spectroscopy experiments, and this facilitates a resonance effect contributing to the Raman intensity of each phonon mode [79]. This effect decreases upon increased temperature due to a larger deviation of the transition energy from the photon energy of the laser light, which results in a lower number of excitonic transitions. This finally leads to reduced intensity of the scattered radiation.

3.5. Thermoelectric properties

The Seebeck coefficient and resistivity for ScN and ScN-T layers determined in the present experiments along with the results of calculations carried out for ScN are shown in Fig. 10. One notices that both computed temperature dependencies of the Seebeck coefficient and resistivity in ScN remain in close agreement with the measured data. The Seebeck coefficient in ScN varies between −30 and −64 μV K^{-1} in ScN, while it is considerably lower in the ScN-T layer, spanning the range from −50 to −82 μV K^{-1} over the temperatures between 300 and 800 K. The resistivity in ScN and ScN-T layers increases as a function of increasing temperature, which indicates that both systems behave as semimetals. The resistivity ranges from 0.21 to 0.39 mΩ cm in ScN and from 0.45 to 0.89 mΩ cm in ScN-T. Hence, the resistivity in the twinned ScN layer is nearly twice as big as that in the almost defect-free ScN layer.

The thermal conductivity measured at room temperature amounts to 10.06 and 2.85 W m^{-1} K^{-1} for ScN and ScN-T, respectively. Again, we find an exceptionally good agreement between the experimental and calculated (10.48 W m^{-1} K^{-1}) thermal conductivity in ScN at room temperature. The calculated thermal conductivity decreases by about 40% in the temperature range of 300 - 800 K, as shown in Fig. 11. The present theoretical study allows us to analyze in more detail the electronic (k_e) and lattice/phonon (k_L) contributions to the overall thermal conductivity (k), especially their temperature dependence. The resulting evolution of k_e and k_L with temperature is depicted in the inset of Fig. 11. We find the phonon term to be about two times higher than the electronic term at room temperature. The k_L decreases, while the k_e increases with temperature. The k_L is the major term in the thermal conductivity up to 500 K, but at higher temperatures, the electronic contribution k_e becomes a dominating term in the heat transfer of ScN. It is also interesting to note that k_L is governed by the acoustic phonons, as the contribution from the optical modes is nearly three orders of magnitude smaller in the entire temperature range covered by our theoretical calculations.

We should also mention that the values of Seebeck coefficient, resistivity, and thermal conductivity of ScN determined in our experimental

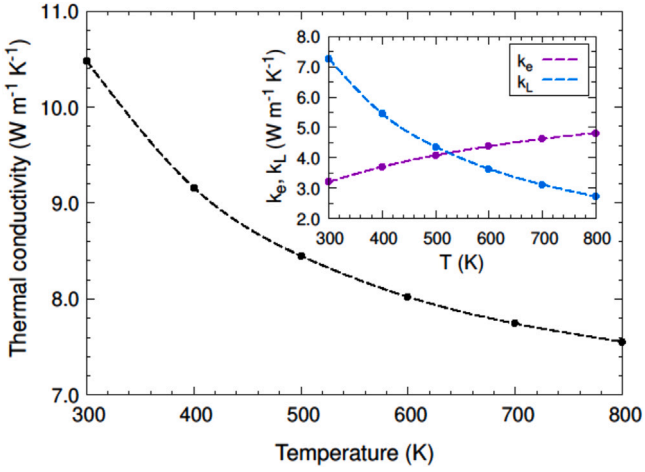

Fig. 11. Calculated temperature dependence of thermal conductivity in ScN. Inset: electronic and lattice contributions to thermal conductivity in ScN.

and theoretical investigations generally correspond to those reported by other studies [19,26,31,33]. The Seebeck coefficient of ScN ranges between −20 and −40 μV K^{-1} at room temperature and between −40 and −160 μV K^{-1} at 800 K. The room temperature resistivity of ScN varies between 0.1 and 1.8 mΩ cm, while the room temperature thermal conductivity of ScN lies in the range 8–12.5 W m^{-1} K^{-2}. Even though stronger Seebeck coefficient at 800 K (−170 μV K^{-1}), lower electrical conductivity (~500 – 1500 Scm^{-1}) as compared to that reported in the present work (~5000 Scm^{-1}), and higher thermal conductivity (~15 W m^{-1} K^{-1}) are sometimes encountered in the literature [24,25,28,32]. Such a spread in the quantities determining thermoelectric properties of ScN can arise from the contamination of samples by a higher amount of oxygen than in our case (~1 – 2%), nitrogen vacancies as well as high-level doping of the scandium sublattice with various elements. All those defects modify the thermoelectric properties of the ScN layers. In particular, oxygen plays an important role as an electron donor, and hence the O-impurities, especially when in high concentration, improve electrical conductivity, and reduce the Seebeck coefficient and thermal conductivity of the ScN films by lowering the k_L term.

Finally, we discuss thermoelectric efficiency to convert heat to electricity, which is governed by the dimensionless figure of merit $ZT = S^2\sigma T/k$, where S, σ, k, and T stand for the Seebeck coefficient, electrical conductivity, thermal conductivity, and temperature, respectively. In fact, the experimentally determined temperature evolution of ZT, which is shown in Fig. 12, is its lower limit, as the value of k has been measured only at room temperature.

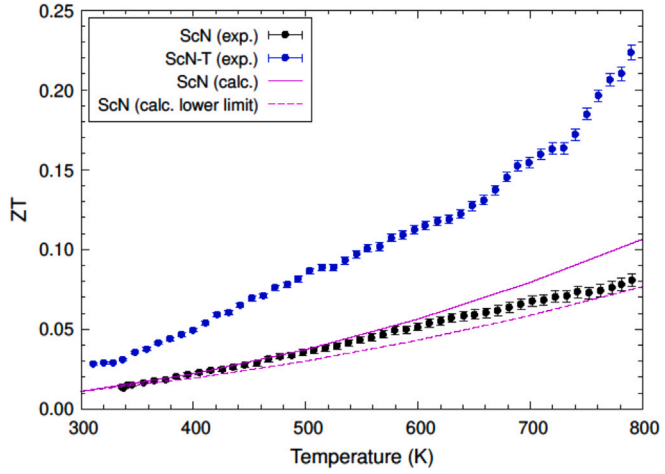

Fig. 12. Lower limit of figure of merit (ZT) as a function of temperature for ScN and ScN-T layers on Mg (001) substrates. Solid (dashed) lines denote calculated ZT (lower limit of ZT) for ScN.

Theoretical temperature dependence of ZT, which is also included in Fig. 12 does not have such limitation, however, to compare with the present experiments the calculated lower limit of ZT is provided as well. Despite some agreement between the calculated and experimental lower limit of ZT in the vicinity of room temperature, the theoretical lower limit of ZT underestimates experimental ZT at elevated temperatures. The experimental lower limit of ZT is approximated better by the calculated *real* ZT up to about 600 K. At still higher temperatures, the lower limit of ZT obtained with the constant value of experimental thermal conductivity measured at room temperature is not sufficient and such approximation suffers from underestimation of *real* ZT. Of course, the higher the temperature the bigger the discrepancy. Nevertheless, the determined values of the lower limit of ZT (0.01–0.03) lie in the range usually reported for ScN films [19,24,28,32,33,85]. The ScN-T layer reveals much higher ZT than the ScN layer, which arises predominantly from the presence of twin domains. They lead to a decrease in thermal conductivity, presumably by suppressing the acoustic phonon propagation, and by lowering the electronic conductivity and enhancing the Seebeck coefficient due to twin domain boundaries.

4. Summary and conclusions

We have undertaken an examination of the microstructural features, dynamical and thermoelectric properties of the ScN/MgO(001) layers produced by the DC reactive magnetron sputtering. In particular, the effect of twin domains on the aforementioned properties of ScN films has been explored. Twin domains were observed in pole figures growing on the 111 twinning planes of the 002-oriented grains. A substantial difference in thermoelectric properties between almost defect-free ScN and that with twin domains is found. Twin domains in the ScN layer give rise to: (i) an increased figure of merit (until at 800 K), (ii) an increased Seebeck coefficient (from −64 to −82 μV K^{-1} at 800 K), and (iii) reduced thermal conductivity (from 10.06 to 2.85 W m^{-1} K^{-1} at 300 K). Thus, a clear improvement in global thermoelectric properties of the ScN films with twin domains is perceived. In both defect-free ScN and that containing twin domains, the quartic anharmonicity of the interatomic potentials is present and reflected by the temperature behavior of their high-frequency optical phonon modes, as revealed by the Raman spectroscopy studies. The results of present research performed on thin ScN epitaxial layers suggest that structural domains can be a rather simple and stable solution enhancing thermoelectric properties of materials in the form of films.

CRediT authorship contribution statement

J. More-Chevalier: Writing – review & editing, Writing – original draft, Visualization, Validation, Supervision, Software, Resources, Methodology, Investigation, Formal analysis, Data curation, Conceptualization. **U.D. Wdowik:** Writing – review & editing, Writing – original draft, Visualization, Validation, Software, Methodology, Investigation, Formal analysis, Data curation, Conceptualization. **J. Martan:** Writing – original draft, Visualization, Validation, Investigation, Formal analysis, Data curation. **T. Baba:** Investigation, Formal analysis, Data curation. **S. Cichoň:** Writing – review & editing, Writing – original draft, Visualization, Validation, Investigation, Formal analysis, Data curation. **P. Levinský:** Visualization, Validation, Investigation, Formal analysis, Data curation. **D. Legut:** Writing – review & editing, Validation, Resources, Project administration, Funding acquisition, Conceptualization. **E. de Prado:** Writing – review & editing, Writing – original draft, Visualization, Validation, Investigation, Formal analysis, Data curation. **P. Hruška:** Validation, Formal analysis, Data curation. **J. Pokorný:** Validation, Formal analysis, Data curation. **J. Bulíř:** Validation, Formal analysis, Data curation. **C. Beltrami:** Visualization, Formal analysis, Data curation. **T. Mori:** Writing – original draft, Visualization, Formal analysis, Data curation. **M. Novotný:** Writing – original draft, Validation, Resources, Project administration, Funding acquisition, Formal analysis, Data curation. **I. Gregora:** Formal analysis, Data curation. **L. Fekete:** Formal analysis, Data curation. **L. Volfová:** Formal analysis, Data curation. **J. Lančok:** Visualization, Resources, Project administration, Funding acquisition, Formal analysis, Data curation.

Declaration of competing interest

The authors declare that they have no known competing financial interests or personal relationships that could have appeared to influence the work reported in this paper.

Acknowledgments

The authors acknowledge the Czech Science Foundation (GAČR) project No. 23-07228S. This work was also supported by the Ministry of Education, Youth and Sports of the Czech Republic through the SENDISO - CZ.02.01.01/00/22_008/0004596 and the e-INFRA CZ (ID:90254). The Interdisciplinary Centre of Mathematical and Computational Modeling (ICM), Warsaw University, Poland is acknowledged for providing computer facilities to perform part of the present calculations.

Appendix A. Formulas to obtain resistivity and thermal conductivity of ScN

The scattering rates $\frac{1}{\tau(\mathbf{k},T)}$ are evaluated according to Ref. [47]

$$\frac{1}{\tau(\mathbf{k},T)} = 4\pi\beta \int_0^\infty \frac{\hbar\omega\, \alpha^2_{\mathrm{tr}\mathbf{k}}(\omega)F(\omega)}{(\exp(\beta\hbar\omega)-1)\,(1-\exp(-\beta\hbar\omega))}\, d\omega, \tag{A.1}$$

where $\beta = \frac{1}{k_B T}$ and $\alpha^2_{\mathrm{tr}\mathbf{k}}(\omega)F(\omega)$ stands for the effective transport phonon frequency distribution computed by the EPW package. In the scattering time approximation, the resistivity $\rho(T)$ can be obtained as:

$$\rho(T) = \frac{m}{ne^2}\left\langle \frac{1}{\tau(\mathbf{k},T)} \right\rangle, \tag{A.2}$$

where m is the electron mass, e denotes its charge, and n is the number of free charge carriers per unit volume. The bracket $\langle\cdots\rangle$ indicates an average over the Fermi surface. The $\rho(T)$ is used to calculate electrical conductivity $\sigma(T) = \rho(T)^{-1}$ and subsequently the electronic contribution to the thermal conductivity k_e from the Wiedemann–Franz law $k_e = k_{e-\mathrm{ph}} = L_0\,\sigma\,T$, with $L_0 = \frac{\pi}{3}\left(\frac{k_B}{e}\right)^2 = 2.44\times10^{-8}$ W Ω K^{-2} denoting the Lorentz number.

The contribution to the lattice thermal conductivity from acoustic phonons k_{La} is calculated according to the Slack model and it takes on the following form [50,51]:

$$k_{La}(T) = k_{La}(\Theta_a)\frac{\Theta_a}{T} \tag{A.3}$$

$$k_{La}(\Theta_a) = A\left(\frac{k_B\Theta_a}{\hbar}\right)^2 \frac{k_B M V^{\frac{1}{3}}}{\hbar\gamma_a^2} \tag{A.4}$$

$$A = \frac{0.849\times 3\sqrt[3]{4}}{20\pi^3(1-0.514\gamma_a^{-1}+0.228\gamma_a^{-2})}, \tag{A.5}$$

where γ_a, M, and V are the overall Grüneisen parameter for acoustic phonon modes, the average atomic mass, and the unit cell volume, respectively. The Θ_a stands for the so-called acoustic Debye temperature, which is related to the Debye temperature Θ_D via the relationship: $\Theta_a = n^{-\frac{1}{3}}\Theta_D$, with n denoting the number of atoms per unit cell. The Θ_a is obtained by considering only the acoustic phonon modes, i.e., under the assumption that the optical phonons do not contribute to heat transport [86]. The Θ_D is derived from the second moment of the calculated phonon spectrum $\langle\mu^2\rangle$ [87]:

$$\Theta_D = \frac{\hbar}{k_B}\sqrt{\frac{5}{3}\langle\mu^2\rangle} \tag{A.6}$$

$$\langle\mu^2\rangle = \frac{\int \omega^2 g(\omega)d\omega}{\int g(\omega)d\omega}, \tag{A.7}$$

where $g(\omega)$ is the computed density of phonon states over the acoustic range. The factor $\frac{\Theta_a}{T}$ is introduced to comply with the observed T^{-1} behavior of the thermal conductivity at temperatures above Θ_D. The γ_a is the weighted average of the $(\mathbf{k}, j)$ mode-specific Grüneisen parameters $\gamma(\mathbf{k}, j)$, where the weighting factors $C_V(\mathbf{k}, j)$ are the contributions of individual acoustic $(\mathbf{k}, j)$ modes to the heat capacity. The following expressions apply:

$$\gamma_a = \frac{\sum_{\mathbf{k},j}\gamma(\mathbf{k},j)C_V(\mathbf{k},j)}{\sum_{\mathbf{k},j}C_V(\mathbf{k},j)} \tag{A.8}$$

$$\gamma(\mathbf{k},j) = -\frac{\partial(\ln\omega(\mathbf{k},j))}{\partial\ln V} = -\frac{V}{\omega(\mathbf{k},j)}\frac{\partial\omega(\mathbf{k},j)}{\partial V}. \tag{A.9}$$

The contribution to the lattice thermal conductivity from optical phonons k_{Lo} is obtained according to the Cahill model [52,53], which is based on the Einstein random walk with the lifetime of each oscillator $\tau = \frac{\pi}{\omega}$, i.e., one half the period of vibration. The k_{Lo} resulting from the random walk between such localized excitations can be expressed as:

$$k_{Lo} = \left(\frac{\pi}{6}\right)^{\frac{1}{3}} N^{\frac{2}{3}}\sum_i v_i\left(\frac{T}{\Theta_i}\right)^2\int_0^{\Theta_i/T}\frac{x^3e^x}{(e^x-1)^2}dx \tag{A.10}$$

$$\Theta_i = v_i\left(\frac{\hbar}{k_B}\right)(6\pi^2 N)^{\frac{1}{3}}, \tag{A.11}$$

where the sum runs over the three sound modes (two transverse and one longitudinal) with speeds of sound v_i. The N and Θ_i denote, respectively, the number density of atoms and the cutoff frequency for each polarization (expressed in degrees Kelvin).

Appendix B. Supplementary data

Supplementary material related to this article can be found online at https://doi.org/10.1016/j.apsadv.2024.100674.

Data availability

The data as well as the figures are available through the following link https://asep.lib.cas.cz/arl-cav/cs/detail-cav_un_epca-0602125-ScN-data/.

References

[1] T. Hendricks, T. Caillat, T. Mori, Advanced thermoelectric generation technologies 2022, Energies 15 (2022) 7307.
[2] M. Mukherjee, A. Srivastava, A.K. Singh, Recent advances in designing thermoelectric materials, J. Mater. Chem. C 10 (2022) 12524–12555.
[3] J.Z. X.-L. Shi, Z.-G. Chen, Advanced thermoelectric design: From materials and structures to devices, Chem. Rev. 120 (2020) 7399–7515.
[4] F. Tohidi, S.G. Holagh, A. Chitsaz, Thermoelectric generators: A comprehensive review of characteristics and applications, App. Therm. Eng. 201 (2022) 117793.
[5] J. Wei, L. Yang, Z. Ma, P. Song, M. Zhang, J. Ma, F. Yang, X. Wang, Review of current high-ZT thermoelectric materials, J. Mater. Sci. 55 (2020) 12642–12704.
[6] L. Jin, Y. Hao, A.K. Tareen, K. Khan, S. Wageh, O.A. Al-Hartomy, A.G. Al-Sehemi, H. Zhang, Y. Zhang, Tellurium/polymers for flexible thermoelectrics: status and challenges, J. Mater. Chem. A 11 (2023) 3771–3788.
[7] F. Hossein-Babaei, S. Masoumi, A. Noori, Linking thermoelectric generation in polycrystalline semiconductors to grain boundary effects sets a platform for novel seebeck effect-based sensors, J. Mater. Chem. A 6 (2018) 10370–10378.
[8] W. Wu, G.-K. Ren, X. Chen, Y. Liu, Z. Zhou, J. Song, Y. Shi, J.-M. Jiang, Y.-H. Lin, Interfacial advances yielding high efficiencies for thermoelectric devices, J. Mater. Chem. A 9 (2021) 3209–3230.
[9] T. Degousée, V. Untilova, V. Vijayakumar, X. Xu, Y. Sun, M. Palma, M. Brinkmann, L. Biniek, O. Fenwick, High thermal conductivity states and enhanced figure of merit in aligned polymer thermoelectric materials, J. Mater. Chem. A 9 (2021) 16065–16075.
[10] H.J. Goldsmid, Introduction to Thermoelectricity, Springer, Berlin, Heidelberg, 2016.
[11] G.J. Snyder, E.S. Toberer, Complex thermoelectric materials, Nature Mater. 7 (2008) 105–114.
[12] M.N. Hasan, H. Wahid, N. Nayan, M.S.M. Ali, Inorganic thermoelectric materials: A review, Int. J. Energy Res. 44 (2020) 6170–6222.
[13] P. Eklund, S. Kerdsongpanya, B. Alling, Transition-metal-nitride-based thin films as novel energy harvesting materials, J. Mater. Chem. C 4 (2016) 3905–3914.
[14] M. Garbrecht, I. McCarroll, L. Yang, V. Bhatia, B. Biswas, D. Rao, J.M. Cairney, B. Saha, Thermally stable epitaxial ZrN/carrier-compensated $Sc_{0.99}Mg_{0.01}N$ metal/semiconductor multilayers for thermionic energy conversion, J. Mater. Sci. 55 (2020) 1592–1602.
[15] B. Saha, T.D. Sands, U.V. Waghmare, First-principles analysis of ZrN/ScN metal/semiconductor superlattices for thermoelectric energy conversion, J. Appl. Phys. 109 (2011) 083717.
[16] V. Rawat, Y.K. Koh, D.G. Cahill, T.D. Sands, Thermal conductivity of (Zr,W)N/ScN metal/semiconductor multilayers and superlattices, J. Appl. Phys. 105 (2009) 024909.
[17] M. Zebarjadi, Z. Bian, R. Singh, A. Shakouri, R. Wortman, V. Rawat, T. Sands, Thermoelectric transport in a ZrN/ScN superlattice, J. Elect. Mater. 38 (2009) 960–963.
[18] R. Kumar, L. Yang, I. McCarroll, S.M. Shivaprasad, J.M. Cairney, M. Garbrecht, B. Saha, Atomistic structure and three-dimensional spatial distribution of oxide clusters along voids in nitride metal/semiconductor superlattices, Phys. Rev. Mater. 5 (2021) 084601.
[19] B. Biswas, B. Saha, Development of semiconducting ScN, Phys. Rev. Mater. 3 (2019) 020301.
[20] R. Deng, B.D. Ozsdolay, P.Y. Zheng, S.V. Khare, D. Gall, Optical and transport measurement and first-principles determination of the ScN band gap, Phys. Rev. B 91 (2015) 045104.
[21] A. le Febvrier, N. Tureson, N. Stilkerich, G. Greczynski, P. Eklund, Effect of impurities on morphology, growth mode, and thermoelectric properties of (111) and (001) epitaxial-like ScN films, J. Phys. D: Appl. Phys. 52 (3) (2018) 035302.
[22] J. More-Chevalier, S. Cichoň, J. Bulíř, M. Poupon, P. Hubík, L. Fekete, J. Lančok, Electrical and optical properties of scandium nitride nanolayers on MgO(100) substrate, AIP Adv. 9 (1) (2019) 015317.
[23] J. More-Chevalier, U.D. Wdowik, D. Legut, S. Cichoň, E. de Prado, I. Gregora, J. Bulíř, M. Novotný, L. Fekete, J. Lančok, Effect of oxygen defects on microstructure, optical and vibrational properties of ScN films deposited on MgO substrate from experiment and first principles, Appl. Surf. Sci. 615 (2023) 156203.
[24] P.V. Burmistrova, J. Maassen, T. Favaloro, B. Saha, S. Salamat, Y. Rui Koh, M.S. Lundstrom, A. Shakouri, T.D. Sands, Thermoelectric properties of epitaxial ScN films deposited by reactive magnetron sputtering onto MgO(001) substrates, J. Appl. Phys. 113 (2013) 153704.
[25] P.V. Burmistrova, D.N. Zakharov, T. Favaloro, A. Mohammed, E.A. Stach, A. Shakouri, T.D. Sands, Effect of deposition pressure on the microstructure and thermoelectric properties of epitaxial ScN(001) thin films sputtered onto MgO(001) substrates, J. Mater. Res. 30 (5) (2015) 626–634.
[26] S. Kerdsongpanya, N. Van Nong, N. Pryds, A. Žukauskaitė, J. Jensen, J. Birch, J. Lu, L. Hultman, G. Wingqvist, P. Eklund, Anomalously high thermoelectric power factor in epitaxial ScN thin films, Appl. Phys. Lett. 99 (2011) 232113.
[27] B. Saha, J.A. Perez-Taborda, J.-H. Bahk, Y.R. Koh, A. Shakouri, M. Martin-Gonzalez, T.D. Sands, Temperature-dependent thermal and thermoelectric properties of n-type and p-type $Sc_{1-x}Mg_xN$, Phys. Rev. B 97 (2018) 085301.

[28] D. Rao, B. Biswas, E. Flores, A. Chatterjee, M. Garbrecht, Y.R. Koh, V. Bhatia, A.I.K. Pillai, P.E. Hopkins, M. Martin-Gonzalez, B. Saha, High mobility and high thermoelectric power factor in epitaxial ScN thin films deposited with plasma-assisted molecular beam epitaxy, Appl. Phys. Lett. 116 (2020) 152103.

[29] S. Kerdsongpanya, B. Sun, F. Eriksson, J. Jensen, J. Lu, Y.K. Koh, N.V. Nong, B. Balke, B. Alling, P. Eklund, Experimental and theoretical investigation of $Cr_{1-x}Sc_xN$ solid solutions for thermoelectrics, J. Appl. Phys. 120 (21) (2016) 215103.

[30] N. Tureson, N. Van Nong, D. Fournier, N. Singh, S. Acharya, S. Schmidt, L. Belliard, A. Soni, A. le Febvrier, P. Eklund, Reduction of the thermal conductivity of the thermoelectric material ScN by Nb alloying, J. Appl. Phys. 122 (2) (2017) 025116.

[31] N. Tureson, M. Marteau, T. Cabioch, N. Van Nong, J. Jensen, J. Lu, G. Greczynski, D. Fournier, N. Singh, A. Soni, L. Belliard, P. Eklund, A. le Febvrier, Effect of ion-implantation-induced defects and Mg dopants on the thermoelectric properties of ScN, Phys. Rev. B 98 (2018) 205307.

[32] D. Rao, O. Chowdhury, A.I.K. Pillai, G.K. Pradhan, S. Sahoo, J.P. Feser, M. Garbrecht, B. Saha, Multifunctional irradiation-induced defects for enhancing thermoelectric properties of scandium nitride thin films, ACS Appl. Energy Mater. 5 (2022) 6847–6854.

[33] R. Burcea, J.-F. Barbot, P.-O. Renault, D. Eyidi, T. Girardeau, M. Marteau, F. Giovannelli, A. Zenji, J.-M. Rampnoux, S. Dilhaire, P. Eklund, A. le Febvrier, Influence of generated defects by Ar implantation on the thermoelectric properties of ScN, ACS Appl. Energy Mater. 5 (2022) 11025–11033.

[34] J. More-Chevalier, S. Cichoň, L. Horák, J. Bulíř, P. Hubík, Z. Gedeonová, L. Fekete, M. Poupon, J. Lančok, Correlation between crystallization and oxidation process of ScN films exposed to air, Appl. Surf. Sci. 515 (2020) 145968.

[35] S. Cichoň, J. More-Chevalier, U.D. Wdowik, E. de Prado, J. Bulíř, M. Novotný, L. Fekete, J. Duchoň, D. Legut, J. Lančok, Environmental stability and ageing of ScN thin films from XPS Ar+ depth profiling, Appl. Surf. Sci. 674 (2024) 160867.

[36] J. Martan, O. Hervé, V. Lang, Two-detector measurement system of pulse photothermal radiometry for the investigation of the thermal properties of thin films, J. Appl. Phys. 102 (2007) 064903.

[37] J. Martan, Optical layer development for thin films thermal conductivity measurement by pulsed photothermal radiometry, Rev. Sci. Instrum. 86 (2015) 014902.

[38] D.L. Balageas, J.C. Krapez, P. Cielo, Pulsed photothermal modeling of layered materials, J. Appl. Phys. 59 (1986) 348–357.

[39] T. Baba, T. Baba, K. Ishikawa, T. Mori, Determination of thermal diffusivity of thin films by applying Fourier expansion analysis to thermo-reflectance signal after periodic pulse heating, J. Appl. Phys. 130 (2021) 225107.

[40] T. Baba, T. Baba, T. Mori, Fourier transform thermoreflectance method under front-heat front-detect configuration, Int. J. Thermophys. 45 (2024) 61.

[41] P. Giannozzi, et al., QUANTUM ESPRESSO: a modular and open-source software project for quantum simulations of materials, J. Phys.: Condens. Matter. 21 (2009) 395502.

[42] P. Giannozzi, et al., Advanced capabilities for materials modelling with quantum ESPRESSO, J. Phys.: Condens. Matter. 29 (2017) 465901.

[43] J.P. Perdew, K. Burke, M. Ernzerhof, Generalized gradient approximation made simple, Phys. Rev. Lett. 78 (1997) 1396.

[44] J. Noffsinger, F. Giustino, B.D. Malone, C.-H. Park, S.G. Louie, M.L. Cohen, EPW: Electron–phonon coupling, transport and superconducting properties using maximally localized wannier functions, Comput. Phys. Commun. 181 (2010) 2140.

[45] S. Poncé, E.R. Margine, C. Verdi, F. Giustino, EPW: Electron–phonon coupling, transport and superconducting properties using maximally localized wannier functions, Comput. Phys. Comm. 209 (2016) 116.

[46] F. Giustino, M.L. Cohen, S.G. Louie, Electron-phonon interaction using wannier functions, Phys. Rev. B 76 (2007) 165108.

[47] B. Hayman, J.P. Carbotte, Anisotropic transport scattering times in the alkali metals, J. Phys. F: Met. Phys. 2 (1972) 915.

[48] M. Bernardi, D. Vigil-Fowler, J. Lischner, J.B. Neaton, S.G. Louie, Ab initio study of hot carriers in the first picosecond after sunlight absorption in silicon, Phys. Rev. Lett. 112 (2014) 257402.

[49] J. Liu, Y. Zhao, C. Lian, Z. Dai, J.-T. Sun, S. Meng, Ab initio study on anisotropic thermoelectric transport in ternary pnictide KZnP, J. Phys.: Condens. Matter. 2 (2019) 024001.

[50] G.A. Slack, Nonmetallic crystals with high thermal conductivity, J. Phys. Chem. Solids 34 (1973) 321.

[51] G.A. Slack, The thermal conductivity of nonmetallic crystals, Solid State Phys. 34 (1979) 1.

[52] D.G. Cahill, R.O. Pohl, Heat flow and lattice vibrations in glasses, Solid State Commun. 70 (1989) 927.

[53] D.G. Cahill, S.K. Watson, R.O. Pohl, Lower limit to the thermal conductivity of disordered crystals, Phys. Rev. B 46 (1992) 6131.

[54] G.K.H. Madsen, J. Carrete, M.J. Verstraete, BoltzTraP2, a program for interpolating band structures and calculating semi-classical transport coefficients, Comput. Phys. Comm. 231 (2018) 140–145.

[55] G. Kresse, J. Hafner, Ab initio molecular dynamics for liquid metals, Phys. Rev. B 47 (1993) 558.

[56] G. Kresse, J. Furthmüller, Efficient iterative schemes for ab initio total-energy calculations using a plane-wave basis set, Comput. Mater. Sci. 6 (1996) 15.

[57] D.B. Zhang, T. Sun, R.M. Wentzcovitch, Phonon quasiparticles and anharmonic free energy in complex systems, Phys. Rev. Lett. 112 (2014) 058501.

[58] T. Sun, D.B. Zhang, R.M. Wentzcovitch, Dynamic stabilization of cubic CaSiO3 perovskite at high temperatures and pressures from ab initio molecular dynamics, Phys. Rev. B 89 (2014) 094109.

[59] D. Gall, I. Petrov, N. Hellgren, L. Hultman, J.E. Sundgren, J.E. Greene, Growth of poly- and single-crystal ScN on MgO(001): Role of low-energy N2+ irradiation in determining texture, microstructure evolution, and mechanical properties, J. Appl. Phys. 84 (1998) 6034–6041.

[60] R.T. Haasch, T.Y. Lee, D. Gall, J.E. Greene, I. Petrov, Epitaxial ScN(001) grown and analyzed in situ by XPS and UPS. I. analysis of As-deposited layers, Surf. Sci. Spec. 7 (2000) 169–177.

[61] R.T. Haasch, T.Y. Lee, D. Gall, J.E. Greene, I. Petrov, Epitaxial ScN(001) grown and analyzed in situ by XPS and ups. II. analysis of Ar+ sputter etched layers, Surf. Sci. Spec. 7 (2000) 178–184.

[62] D. Gall, I. Petrov, P. Desjardins, J.E. Greene, Microstructural evolution and Poisson ratio of epitaxial ScN grown on TiN(001)/MgO(001) by ultrahigh vacuum reactive magnetron sputter deposition, J. Appl. Phys. 86 (1999) 5524–5529.

[63] B.W. Karr, I. Petrov, D.G. Cahill, J.E. Greene, Morphology of epitaxial TiN(001) grown by magnetron sputtering, Appl. Phys. Lett. 70 (1997) 1703–1705.

[64] F.F. Leal, S.C. Ferreira, S.O. Ferreira, Modelling of epitaxial film growth with an Ehrlich–Schwoebel barrier dependent on the step height, J. Phys.: Condens. Matter. 23 (2011) 292201.

[65] S.C. Wang, G. Ehrlich, Adatom motion to lattice steps: A direct view, Phys. Rev. Lett. 70 (1993) 41–44.

[66] R. Dheemahi, B. Bidesh, A. Shashidhara, B. Vijay, P.A.I. Kamalasanan, G. Magnus, S. Bivas, Effects of adatom mobility and Ehrlich–Schwoebel barrier on heteroepitaxial growth of scandium nitride (ScN) thin films, Appl. Phys. Lett. 117 (2020) 212101.

[67] G. Travaglini, F. Marabelli, R. Monnier, E. Kaldis, P. Wachter, Electronic structure of ScN, Phys. Rev. B 34 (1986) 3876.

[68] D. Gall, M. Stoehr, J.E. Greene, Vibrational modes in epitaxial $Ti_{1-x}Sc_xN$(001) layers: An ab initio calculations and Raman spectroscopy study, Phys. Rev. B 64 (2001) 174302.

[69] R. Deng, K. Jiang, D. Gall, Optical phonon modes in $Al_{1-x}Sc_xN$, J. Appl. Phys. 115 (2014) 013506.

[70] M. Balkanski, R.F. Wallis, E. Haro, Anharmonic effects in light scattering due to optical phonons in silicon, Phys. Rev. B 28 (1982) 1928.

[71] J. Menéndez, M. Cardona, Temperature dependence of the first-order Raman scattering by phonons in Si, Ge, and alpha-Sn: anharmonic effects, Phys. Rev. B 29 (1982) 2051.

[72] J. González, E. Moya, J.C. Chervin, Anharmonic effects in light scattering due to optical phonons in $CuGaS_2$, Phys. Rev. B 54 (1996) 4707.

[73] A.A. Maradudin, A.E. Fein, Scattering of neutron by an anharmonic crystal, Phys. Rev. B 128 (1962) 2589.

[74] L. Ciprian, S. Mihalic, C. Lüttich, F. Hörich, E. Wade, B. Christian, A. Dadgar, O. Ambacher, Thermal expansion coefficient of ScN(111) thin films grown on Si(111) determined by X-ray diffraction, Appl. Phys. Lett. 124 (2024) 052203.

[75] S. Tahri, A. Qteish, I.I. Al-Qasir, N. Meskin, Vibrational and thermal properties of ScN and YN: quasi-harmonic approximation calculations and anharmonic effects, J. Phys.: Condens. Matter. 24 (2011) 035401.

[76] I. Antoniazzi, N. Zawadzka, M. Grzeszczyk, T. Woźniak, J.I. nez, Z. Muhammad, W. Zhao, M.R. Molas, A. Babiński, The effect of temperature and excitation energy on Raman scattering in bulk HfS_2, J. Phys.: Condens. Matter. 35 (2023) 305401.

[77] J. Peng, S. Najmaei, M. Dubey, P.W. Chung, A reversible structural transition at 300 K to a low-symmetry polytype of hafnium disulfide atomic layer, Mater. Today Commun. 26 (2021) 101722.

[78] S. Mann, V.K. Jindal, Blue and red shifted temperature dependence of implicit phonon shifts in graphene, Mater. Res. Express 4 (2017) 075038.

[79] H. Zobeiri, S. Xu, Y. Yue, Q. Zhang, Y. Xie, X. Wang, Effect of temperature on Raman intensity of nm-thick WS_2: combined effects of resonance Raman, optical properties, and interface optical interference, Nanoscale 12 (2020) 6064–6078.

[80] S. Xie, E. Iglesia, A.T. Bell, Effects of temperature on the Raman spectra and dispersed oxides, J. Phys. Chem. B 105 (2001) 5144–5152.

[81] Z. Zhao, J. Elwood, M.A. Carpenter, Phonon anharmonicity of PdO studied by Raman spectrometry, J. Phys. Chem. C 119 (2015) 23094–23102.

[82] H. Malekpour, A.A. Balandin, Raman-based technique for measuring thermal conductivity of graphene and related materials, J. Raman Spectrosc. 49 (1) (2018) 106–120.

[83] A. Özden, E. Zuñiga-Puelles, J. Kortus, R. Gumeniuk, C. Himcinschi, Thermal conductivity and phonon anharmonicity of chemical vapor transport grown and mineral–FeS_2 single crystals: An optothermal Raman study, J. Raman Spectrosc. 54 (1) (2023) 84–92.

[84] Q. Xie, L. Xu, C. Hu, L. Chen, J. Zheng, W. Wang, H. Yin, G. Cheng, X. Ai, Phonon anharmonicity of thermoelectric material $HfTe_5$ studied by Raman spectroscopy, J. Raman Spectrosc. 52 (5) (2021) 988–994.

[85] B. Saha, T.D. Sands, U.V. Waghmare, Thermoelectric properties of HfN/ScN metal/semiconductor superlattices: a first-principles study, J. Phys.: Condens. Matter. 24 (41) (2012) 415303.
[86] D.T. Morelli, G.A. Slack, High lattice thermal conductivity solids, in: High Thermal Conductivity Materials, Springer, New York, 2006, p. 37.
[87] G. Grimvall, Thermophysical Properties of Materials, Elsevier, 1999.